DOI: 10.31534/engmod.2023.1.ri.04a
Preliminary communication
Received: 17.10.2022.

Containment Lining Solutions and Hydrodynamic Stability of Tailings Dam

Violeta Mircevska(1*), **Ana Nanevska**(1), **Miroslav Nastev**(2), **Trajce Zafirov**(1)

(1*) *Institute of Earthquake Engineering and Engineering Seismology, University of "Ss. Cyril and Methodius", Todor Aleksandrov Str., 165, P.O. Box 101, 1000 Skopje, R.N. MACEDONIA*

e-mail: violeta@iziis.ukim.edu.mk (corresponding author)

(1) *Institute of Earthquake Engineering and Engineering Seismology, University of "Ss. Cyril and Methodius", Todor Aleksandrov Str., 165, P.O. Box 101, 1000 Skopje, R.N. MACEDONIA*

e-mails: nanevska@iziis.ukim.edu.mk; trajce@iziis.ukim.edu.mk

(2) *Natural Resources Canada, Geological Survey of Canada, Quebec City, CANADA G1K 9A9*

e-mail: miroslav.nastev@canada.ca

SUMMARY

The study investigates the impact of reservoir lining on the hydrodynamic stability of a tailings dam. A 3D coupled fluid-solid finite element model was used for detailed seepage analyses based on conventional flow-net and steady seepage conditions. Pore pressure, stationary seepage velocities, static liquefaction and the ratio between manifested and critical hydraulic gradients were predicted under three different lining conditions. The highest potential for internal erosion and heave was observed in the lined reservoir and starter dam scenario. Although there are environmental benefits, the incorporation of liners in dam design requires a comprehensive engineering assessment of the negative hydrodynamic effects.

KEY WORDS: *hydrodynamic stability; tailings dam; stationary seepage; critical erosion zones; heave potential.*

1. INTRODUCTION

Tailings dams are built progressively in stages integrating by-products of mineral extraction and mine wastes as the main fill material. Their safety and stability vary during and after the construction and operational phases mainly due to the slow consolidation settlement accompanied by pore pressure dissipation [1]. To prevent failures and eventual environmental impacts, the tailings dams have to be designed to satisfy rigorous criteria for long-term stability with a minimal maintenance effort. A dam's safety and stability can be analysed using coupled fluid-solid mathematic models that consider steady seepage with conventional flow net analysis [2, 3] and a finite element approach to the assessment of the stress field based on reliable constitutive material models [4].

A simple statistical analysis indicates that, over the last ten years, the number of destructive failures has been of a similar rate of occurrence as those ten years before [5]. In addition, the prohibitive costs of monitoring and post-closure maintenance could sometimes jeopardize the dam's safety [6, 7]. In the past 100 years, the failure rate of tailings dams was estimated at about 1.2%., while the failure rate of the EWRDs was only 0.01% [8]. The evidence gained from tailings dam failures indicates that the main reasons have been internal erosion due to uncontrolled seepage and/or piping (21.6%), overtopping (20.6%), foundation failure (17.3%), seismic shaking and liquefaction (17.0%), followed by dam subsidence, structural and slope instability, etc. [9]. Another review of tailings dam failure carried out by Foster et al. [10], showed that about 30% of the worldwide considered failures of large tailings dam embankments resulted from erosion, piping, and heave effects.

A recent worldwide overview of tailings dam failures points out insufficient progress in the development of tailings dams safety standards, guidelines, risk assessment, and management tools. Currently, most of the design requirements for tailings dams are based on design principles and knowledge of the behaviour of the conventional earth dams, whereas only a few issues specific to the tailings dam design and safety are addressed explicitly, ANCOLD 2012 [11] and CDA 2014 [12]. However, besides the numerous similarities, considerable differences exist between the tailings and conventional earth dams. The tailings dams are raised in stages, progressively with the mining activities, which can extend over several decades. They are built of silt-to-sand-sized material with significantly different properties than the natural soils of the earth dams, e.g., grain size, compaction, and relative density.

One of the most important factors related to the stability and long-term performance of tailings dams is certainly the prevention of internal erosion, manifested by piping and heave, i.e., migration of finer particles initiated by seepage pressure. If the erosion is left to develop freely, a preferential seepage pathway is created through which seepage water and fine particles move freely to a free exit. This process is accompanied by a change in the tailings' material properties, such as increased permeability and decreased shear strength and modulus of deformation. The seepage rate, at the same time, is correlated to the elevation of the phreatic surface, hydraulic gradient, grain size distribution, the advancement of the consolidation process, internal structure, etc. [13, 14]. For example, tailings with low hydraulic conductivity undergo slow consolidation that may result in an increase of the pore pressure and a possibility of the formation of erosion channels, particularly within the finer materials [15]. Seepage barriers in the form of the lining (impermeable membrane) are commonly used for environmental purposes to prevent uncontrolled leaching and release of toxic compounds into the surface and groundwater. If not installed properly or if the lining deforms and cracks, the high differential pressures across the lining decrease its effectiveness and may initiate erosion of the adjacent soil [16].

The objective of the present study is to investigate the impacts of impermeable lining systems on the hydrodynamic stability of tailing dams. Existing 72 m high tailings dam, at its final operational phase, is taken as an example. The dam was built with a modified downstream method with a support stone fill at the lower part of the downstream slope. Two lining options were considered: lining of the reservoir walls, bottom, and the upstream slope of the starter dam; and lining of the reservoir walls and bottom only. The third option considered for comparison was the conventional dam design without any lining. The finite element method was used to model the stress field under static loads and seepage forces for different seepage boundary conditions. The evaluation of the stress tensor was based on the finite element analysis applying the Mohr-Coulomb material model as a "first order" approximation of the soil

elasto-plastic behaviour. The focus was on the impacts of the liner solutions on the potential of hydraulic failure triggered by internal erosion and the potential of heave liquefaction.

2. BACKGROUND

2.1 HYDRODYNAMIC SOIL DEFORMATION

At sufficiently high hydraulic gradients, tailing dams may be subjected to permanent hydrodynamic deformations as a result of the mobilization of soil particles, such as erosion, suffusion, and heave effect. Numerous studies identified internal erosion due to poor compaction, differential settlement, frost action, desiccation, etc., as one of the main forms of hydrodynamic deformation behind failures of earth structures [10]. A special case of erosion is backward erosion, where the material first starts to erode at the free unfiltered exit of the seepage path followed by retrograde erosion, which may continue all the way to the dam`s upstream slope [17]. Piping refers to internal erosion along a seepage pathway with a formation of a low-pressure conduit allowing concentrated flow. Piping with sufficient velocity to erode the embankment face may generate local or general failure of the embankment [18]. Suffusion, on the other hand, is a type of erosion process occurring in internally unstable materials and manifested with selective dislodging of the fine particles from the coarser soil skeleton whose volume remains unchanged [18]. Taking place mainly in soils with bimodal structure, the suffusion gradually decreases the density and the coefficient of uniformity, increasing the porosity and the hydraulic conductivity and creating conditions favourable for internal erosion.

The soil stability can also be compromised with the progressive decrease of the stress tensor as the pore pressure increases. The strength loss occurs because of the contractive nature of the loaded loose soil. Since the contraction is not allowed due to the incompressibility of the pore water, outward stresses are generated as counteraction which decreases soil stresses. The undrained soft and loose soils are as well prone to the effect of flow liquefaction resulting from the strain softening behaviour concomitant with continuous reduction of the shear resistance and additional plastic shear strains [19]. During the stationary seepage in soft, loose, and mainly contractive soils, the outward pore pressures could eventually reduce the total mean and/or the total vertical stress generating a concentrated heave, also known as a blowout. The static liquefaction is provoked, in general, by triggering mechanisms such as overloading (rapid raising rate, construction activities at crest), changes in pore pressure (rapid construction rate, intense rainstorms, high pond levels), overtopping, as well as by the reduction of lateral confinement (due to erosion) of the downstream slope [20].

2.2 CRITICAL HYDRAULIC GRADIENT

The hydrodynamic deformation processes and the embankment stability are directly related to the seepage rate. The potential of piping failure is determined by comparing the actual hydraulic gradient to the evaluated critical hydraulic, emphasizing the need for accurate knowledge of the expected critical hydraulic gradient. Traditionally, its assessment is based on empirical evidence in field conditions, laboratory measurements, and theoretical and analytical studies. A significant amount of research has been done studying quantitatively the hydraulic gradients critical to trigger internal erosion and their limit values for which the shear strength of confined soil is reduced by drag forces of the seeping water. Indraratna et al. [21] proposed a practical definition

of the critical gradient as the ratio between the buoyant unit weight of soil and the unit weight of water. However, such a definition may be quite inaccurate since the critical gradient in piping depends on inherent soil properties, such as grain size, gradation, porosity, interparticle friction as well as the boundary friction, compaction, interlocking effect of the angular soil particles, etc. [17]. Gravity has also a significant influence on material transport, and it is important to consider the flow direction, i.e., horizontal, upward, or downward flow. Richards et al. [22] developed a true triaxial piping test apparatus to measure the critical hydraulic gradient and the initiating critical velocity at which piping in cohesionless soil begins. The authors investigated the relationship between the seepage direction and gravity and demonstrated that the critical velocity provides more valuable information on piping initiation than the critical gradient. On the other hand, Wan et al. [23] introduced hole erosion and slot erosion tests to study erosion characteristics, such as the erosion rate index and the critical erosion shear stress at which erosion begins. Investigating the piping erosion in the sand, confirmed the increase of the critical hydraulic gradient with increased particle size and hydraulic conductivity of the material, and defined the correlation between the critical gradient and the coefficient of uniformity C_u [24]. The recent experimental study by Quanyi et al. [25] considered the internal erosion in homogeneous materials as a function of the degree of compaction and particle roughness, where the soil compaction and clay content contributed to the increase of the critical hydraulic gradient from 10 to up to 70%. Jahanzaib et al. [26] conducted experimental investigations to quantify the critical hydraulic gradients in internally unstable non-uniform sand and gravel mixtures and stable uniform fine sands. It was concluded that for upward flow in unstable soil, the critical hydraulic gradients are lower than unity. It was also found that the relative density in stable soils has a strong effect on the critical hydraulic gradients. Wan et al. [27] modified the expression for the critical hydraulic gradient, as given by Terzaghi et al. [28] introducing a hydraulic gradient at which particle erosion and boiling begin. In this paper, the critical hydraulic gradient is assessed considering the relatively simple expression of Perzlmaier [29] where two different critical gradients were considered for flow to an unfiltered exit and for flow within the soil matrix. The critical gradient for the unfiltered exit, i_{crit}, is:

$$i_{crit} = \frac{(1-n)(\gamma_s-\gamma_w)}{\gamma_w} \quad \textbf{(1)}$$

where n is porosity, γ_s is the specific weight of soil, and γ_w is the specific weight of water. For seepage throughout the soil matrix, the critical gradient value is reduced in the range from 70 to 80% of the critical gradient for the unfiltered exit.

The criterion for suffusion according to Perzlmaier [29] is correlated positively to the coefficient of uniformity, c_u, indicating a higher risk for suffusion with the increase of c_u as follows in Eq. (2):

$$i_{crit} = \begin{Bmatrix} 0{,}3\ to\ 0{,}4 & for & C_u < 10 \\ 0{,}2 & for & 10 \le C_u \le 20 \\ 0{,}1 & for & C_u > 20 \end{Bmatrix} \quad \textbf{(2)}$$

3. FINITE ELEMENT ANALYSIS OF SEEPAGE

The stationary seepage is the most common during dam serviceability occurring under steady-state conditions with constant pore pressure. The pore pressure contributes to the reduction of total stresses accompanied by negligible deformations. The equation of continuity that governs the stationary seepage process can be written as follows:

$$\frac{\partial}{\partial x}\left(k_{xx}\frac{\partial W}{\partial x}\right) + \frac{\partial}{\partial y}\left(k_{yy}\frac{\partial W}{\partial y}\right) + \frac{\partial}{\partial z}\left(k_{zz}\frac{\partial W}{\partial z}\right) = 0 \quad \textbf{(3)}$$

where $W(x, y, z)$ is the potential function, and k_{xx}, k_{yy}, k_{zz} are Darcy's permeability coefficients in the global x, y, and z directions. Two boundary condition types can be imposed along the contours of the seepage medium:

- Essential boundary condition that prescribes the potential acting along the surface contour S_1:

$$W = \bar{W} \tag{4}$$

- Natural boundary condition that determines the velocity V_n in direction of the normal n of the surface contour S_2:

$$V_n = -\left(k_{xx}\frac{\partial W}{\partial x}\cos(nx) + k_{yy}\frac{\partial W}{\partial y}\cos(ny) + k_{zz}\frac{\partial W}{\partial z}\cos(nz)\right) = \bar{V_n} \tag{5}$$

where cosine functions define the direction of the normal with respect to the global coordinate system. The projections of seepage velocity in the case of incompressible fluid in a three-dimensional orthotropic medium (V_x, V_y, V_z) are also described by Darcy's law:

$$V_x = -k_{xx}\frac{\partial W}{\partial x};\ V_y = -k_{yy}\frac{\partial W}{\partial x};\ V_z = -k_{zz}\frac{\partial W}{\partial z} \tag{6}$$

To transform the integral expression of the analysed problem in a form suitable for application with the finite element method, the system of Eqs. (3), (4) and (5) can be solved either with the weighted residual method, the variation method, or as proposed herein, with the method of virtual work:

$$\iiint_{\Omega}\left(k_{xx}\frac{\partial W}{\partial x}\frac{\partial \delta W}{\partial x} + k_{yy}\frac{\partial W}{\partial y}\frac{\partial \delta W}{\partial y} + k_{zz}\frac{\partial W}{\partial z}\frac{\partial \delta W}{\partial z}\right)dxdydz = \iint_{S2}\bar{V_n}\delta W ds = 0 \tag{7}$$

Explicit integration of Eq. (7) may be difficult and often impossible, especially when the seepage domain, Ω, is of complex geometry. Therefore, numerical integration is applied to transform the volume and surface integrals of Eq. (7) in an equivalent ensemble of discrete finite domains, Ω_i. Herein, the seepage domain is discretized with a number of 3D seepage finite elements, while the surface domain is divided into 2D sub-surfaces as follows:

$$\sum_{i=1}^{NEL}\int_{\Omega_i}\left(k_{xx}\frac{\partial W}{\partial x}\frac{\partial \delta W}{\partial x} + k_{yy}\frac{\partial W}{\partial y}\frac{\partial \delta W}{\partial y} + k_{zz}\frac{\partial W}{\partial z}\frac{\partial \delta W}{\partial z}\right)d\Omega - \sum_{i=1}^{NEL}\int_{S_2}\bar{V_n}\delta W ds = 0 \tag{8}$$

where NEL is the number of finite elements constituting the seepage domain Ω.

4. EXAMPLE TAILINGS DAM

Herein, an existing large tailings dam built with a variant of the downstream method with a support stone fill on the downstream side is considered (Figure 1).

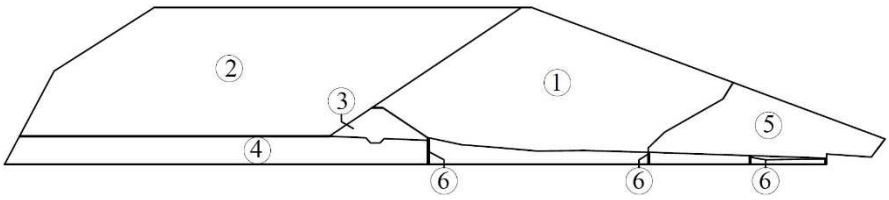

Fig. 1 *Cross-section of the tailings dam: 1) downstream sand embankment, 2) tailings pond, 3) symmetric, homogeneous starter dike made of graphite shale, 4) gravel with variable thickness (8-10m), 5) downstream rockfill support, 6) drainage carpet with drainage pipes*

The dam represents the lowest part of a cascade system of four tailings dams built in a solid rock canyon. The tailings pond is enclosed by the canyon walls, the downstream slope of the upper

tailings dam and the upstream slope of the sand embankment and the initial dike of the actual dam. The tailings material was placed hydraulically with mobile cyclones located on the dam crest. The structural height of 72 m includes the underlying riverbed sediments about 8 m thick. The bottom width of the tailings dam-impoundment system is 406 m, the crest is 5 m wide, and the upstream and downstream slopes of the sand embankment are 1:1.5 and 1:2.7, respectively, Figure 2.

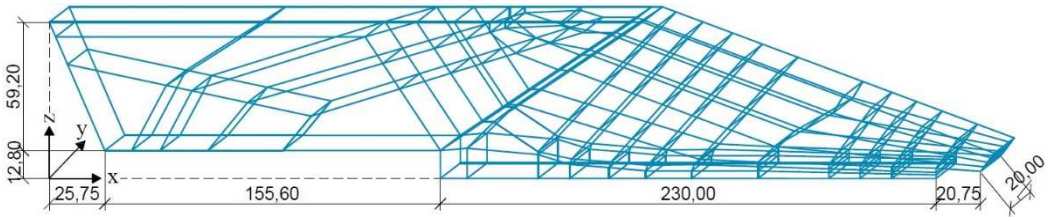

Fig. 2 *3D model of the tailings dam*

The seepage boundary conditions and the permeability of the different soil layers, foundation and impoundment determine the level of the phreatic line. In this way, these parameters directly impact the seepage forces, seepage velocities, pore pressure distribution and the potential for internal instability within the complex tailings dam-impoundment system. To quantify those impacts under different options of impermeable lining, three models of 3D isotropic stationary seepage were analysed: i) Model A: the lining of the reservoir walls, reservoir bottom and the upstream slope of the starter dam; ii) Model B: the lining of the reservoir walls and bottom only; iii) Model C: no lining applied.

The tailings dam FE model was composed of 220 substructures and 22,000 finite elements. Each 3D substructure was discretized with 100 finite elements adopting five divisions in the x and z directions and four divisions in the y direction (20 m long). The seepage boundary conditions assigned with respect to the assumed referent coordinate system for models A, B and C are shown in Figure 3.

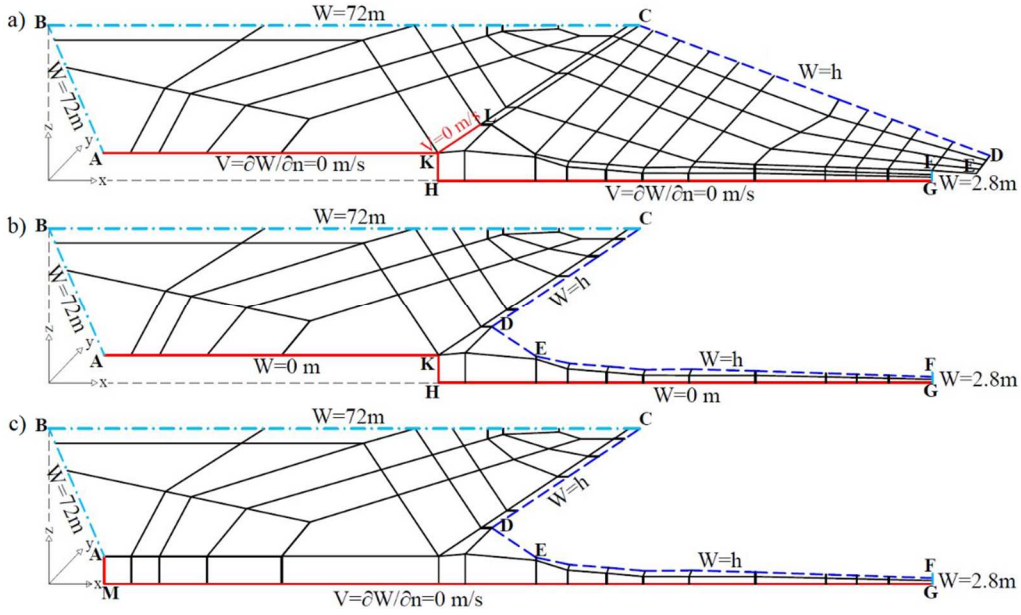

Fig. 3 *Seepage boundary conditions for a) model A, b) model B, and c) model C. Boundary conditions are imposed constant potential (dot-dashed light blue line); phreatic line exposed to atmospheric pressure (dashed blue line), restricted seepage (bold red line), and undisturbed seepage (elsewhere)*

In all three models, the free impoundment surface BC and the back-terrain surface AB are assigned a constant potential of W=72 m. In model A, the dam downstream face is exposed to atmospheric pressure and closely mimics the phreatic surface, with the potential of each point equal to the geostatic height, $W=h$. In the case of models B and C, the phreatic surface goes along the sand embankment upstream slope, the starter dam downstream slope, and the bottom of the sand embankment. The bottom lining is assigned zero seepage velocities in models A (including the upstream face of the starter dam) and B, whereas in model C undisturbed water seepage is enabled through the bottom of the impoundment, the gravel layer below the dam and the starter dike. The distribution of hydraulic conductivities across the layers representing the tailings impoundment, starter dike, sand embankment, stone support fill, and the gravelly base are given in Figure 4 and Table 1.

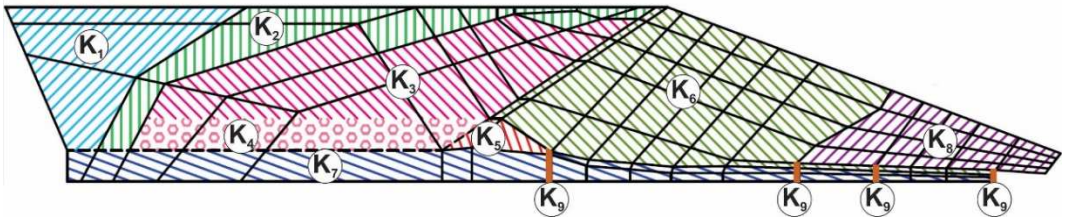

Fig. 4 *Hydraulic conductivity of the distinct zones of the tailings dam-impoundment system*

Table 1 *Hydraulic conductivity of the distinct zones (shown in Figure 4)*

Zone	*Description*	*Isotropic hydraulic conductivity Kx=Ky=Kz (m/s)*	*Porosity N*	*γ_s [kN/m³]*	*Youngs modulus Es [kPa]*
1	*tailings pond*	*K_1=0.001*	*Na*	*Na*	*Na*
2	*tailings pond*	*K_2=0.00005*	*Na*	*Na*	*29,000*
3	*tailings pond*	*K_3=0.0000015*	*Na*	*Na*	*36,000*
4	*tailings pond*	*K_4= 0.000001*	*Na*	*Na*	*45,000*
5	*starter dike*	*K_5=0.0000001*	*0.289*	*27.0*	*90,000*
6	*sand embankment*	*K_6=0.000002*	*0.3-0.483*	*32.0*	*43,000-75,000*
7	*natural sediments*	*K_7=0.0001*	*0.283*	*26.5*	*100,000*
8	*stone fill*	*K_8=0.00001*	*0.315-0.375*	*32.0*	*25,000-57,000*
9	*drainage*	*K_9=0.001*	*Na*	*Na*	*Na*

5. RESULTS OF STATIONARY SEEPAGE ANALYSES

The finite element calculations were run with the ADAD-IZIIS software [30] for static and dynamic analyses of earth and concrete dams. Six major outputs are discussed herein: (i) potential field, (ii) pore pressure distribution, (iii) velocity of seepage, (iv) manifested (actual) and critical hydraulic gradients, (v) static stresses, and (vi) piping and static liquefaction (heave effect) potentials. It is assumed that the seepage conditions of the analysed 3D models are invariable in the direction perpendicular to the central cross section, and the presented results are valid only for the portion of the tailings dam near that section only.

5.1 POTENTIAL

Figure 5 presents the distribution of the potential field, across the dam-impoundment seepage domain. In general, the potential fields of the three models agree well with the predefined seepage boundary conditions (Figure 3). Since tailings are considered fully saturated with water, the maximum equipotential line, equal to the dam height of 72 m, extends at the free water surface. The minimum potential of 2.8 m is simulated at the downstream edge of the model where seepage enters the outlet channel. For the sake of better visual clearance, the disposition of certain characteristic equipotential values is also separately shown in Figure 5. In the case of model A, the highest gradient of the potential field can be observed in the sand embankment and the starter dike, (Figure 5a). In the tailings impoundment, the potential drop is considerably lower, i.e., decreasing from 72 m at the free water surface to about 60 m at the starter dike crest. A discontinuity of the equipotential lines at the interface between the tailings and starter dike is easily observable since the seepage through the upstream slope of the starter dike is prevented by the impermeable lining. The pressure potentials in models B and C are similar and the equipotential lines at the contact zone between the tailing impoundment and the starter dike are continuous (Figure 5b and Figure 5c). Contrary to model A, the considerably shorter seepage path results in a much higher gradient of the potential in the tailings, dropping from 72 m down to 30 m. The remaining potential vanishes within the starter dike and the drainage carpet. The only noticeable difference between models B and C is a consequence of the allowed seepage through the natural sediments (coarse alluvium, gravels) at the base of the tailings pond in model C. In this case, the vertical equipotential lines indicate practically horizontal flow due to the assumed considerably higher permeability in the natural sediments, (Figure 5c).

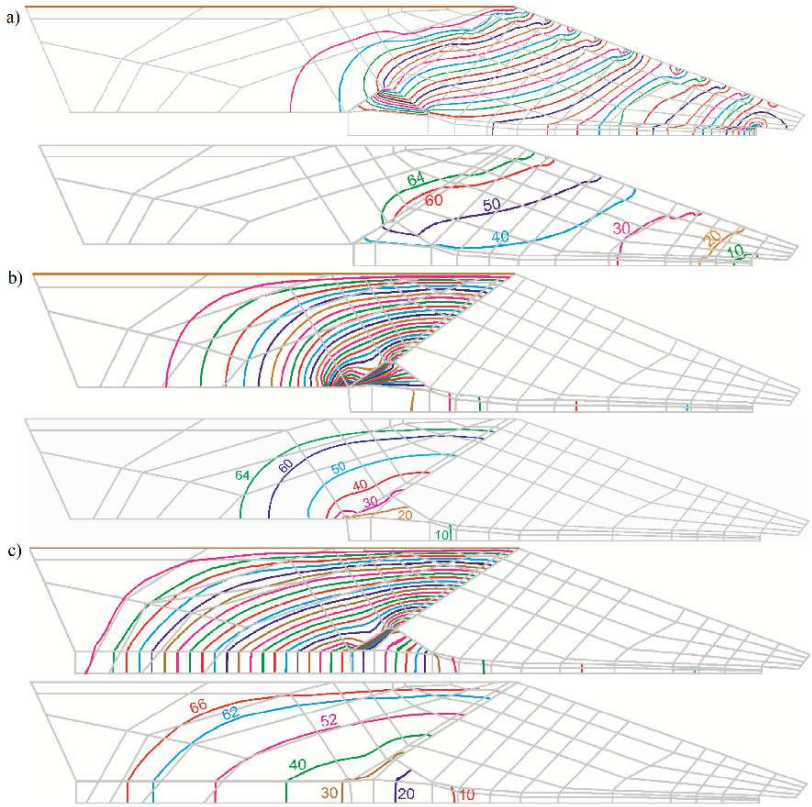

Fig. 5 *Distribution of the potential fields throughout the seepage domain (equidistance 2 m) and selected equipotential lines for a) model A, b) model B, and c) model C*

5.2 PORE WATER PRESSURE

The distributions of the pore pressure field throughout the seepage domain in the form of isobars corresponding to the characteristic pore pressures are illustrated in Figure 6. Zero pore pressure or atmospheric pressure acts along the phreatic surface. It increases with depth, attaining the maximum value of about 590 kPa at the bottom of the tailings pond in all three models. In the case of model A, the continuity of the isobaric lines is disrupted again at the interface with the starter dike.

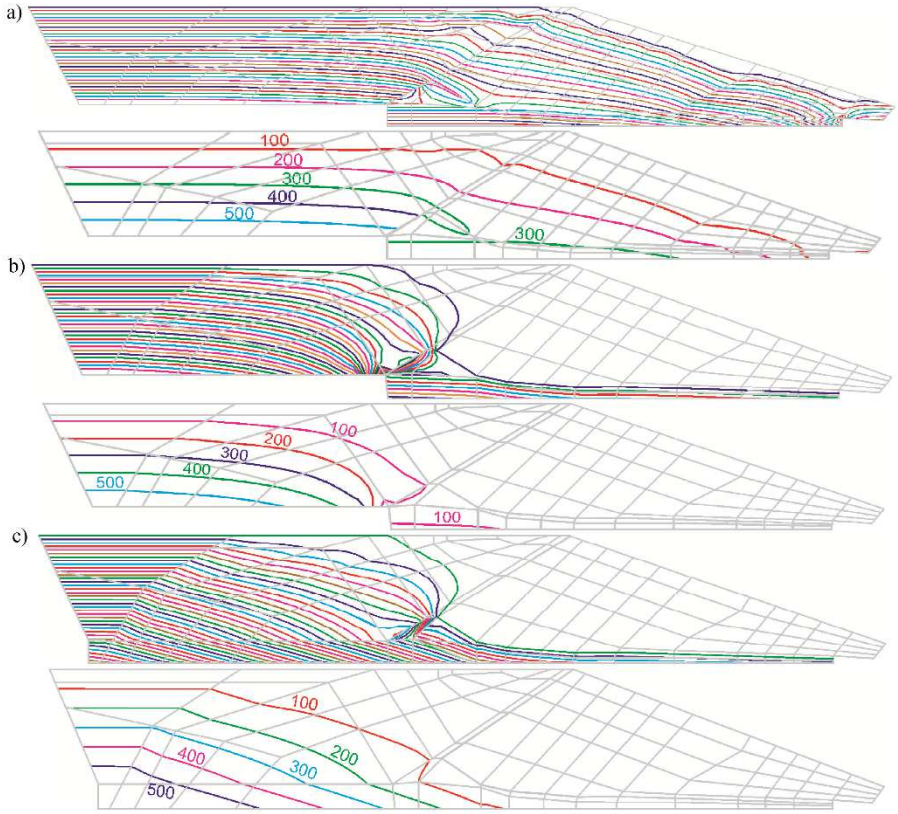

Fig. 6 *Distribution of pore pressure through the seepage domain in [kPa] (equidistance of 20 kPa) and selected pore pressure isobars for a) model A, b) model B, and c) model C*

Whereas in model A the pore pressure increase is practically constant, going towards the lower part of the tailings pond, (Figure 6a), in models B and C, the pressure gradually increases from about 100 kPa at the starter dike to the maximal value of 590 kPa at the downstream slope of the upper tailings dam (Figure 6b and Figure 6c). In model C, the pore pressure in the impoundment increases further in the underlying natural sediments, attaining a value of 720 kPa, (Figure 6c).

5.3 SEEPAGE VELOCITIES

The visualization of the seepage velocities is given in the form of vectors in Figure 7, Figure 8, and Figure 9. The length of the vectors indicates velocity magnitude, whereas the arrows point out the seepage direction. To get a better insight into the seepage velocity distribution, it is given for the characteristic parts of the tailings dam-impoundment system, whose location and extent are indicated in red.

Model A: the installation of impermeable lining and the respective no-flow boundary along the bottom of the impoundment and the upstream face of the starter dike contribute to the development of predominantly horizontal flow with relatively low seepage velocities just above the bottom lining. Close to the upstream slope of the starter dike, the seepage velocities increase and gradually circumvent the dike (Figure 7b). Then, the seepage water overtops the starter dike and merges with the general seepage flow toward the sand embankment (Figure 7c). The significant potential variation just above the starter dike results in an increase in the seepage velocity to 2.1 x 10^{-6} m/s. In contrast, the seepage velocities in the starter dike are with significantly smaller magnitude of extreme magnitude at the crest of about 0.5 x 10^{-6} m/s. In the sand embankment, the velocities vary in the range of 1~5.4 x 10-6 m/s. There, the maximum velocity of 5.4 x 10^{-6} m/s is manifested at the interface starter dike-sand embankment-vertical drain. The higher permeability of the supporting stone fill and the drain carpets contribute to a subsequent increase of the seepage velocities, 31 x 10^{-6} m/s in the supporting stone fill (at the entrance in the outlet channel), while the overall maximum velocity of 101 x 10^{-6} m/s occurs within the drain carpet (Figure 7d and Figure 7e).

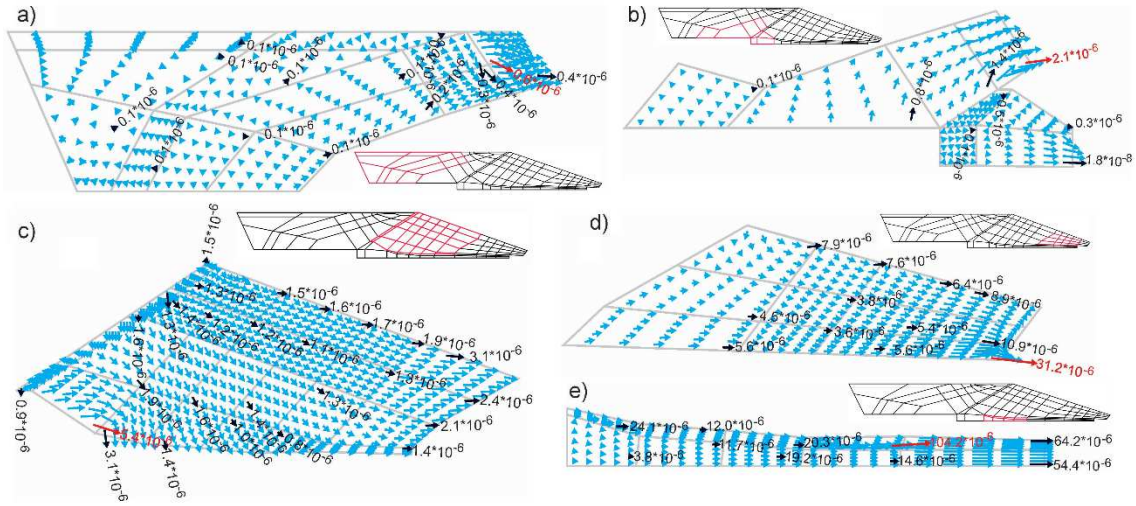

Fig. 7 *Model A: Velocity of seepage (m/s) in characteristic parts of the seepage domain. The maximum velocity value is indicated in red*

Model B: as a consequence of the abrupt potential drop along the shorter path length the seepage velocities are considerably higher than those of model A. In the tailings pond, the extreme seepage velocities occur at the reservoir bottom adjacent to the starter dike, where the highest gradient of potential is manifested (Figure 8a). There, the maximum velocity of 19 x 10^{-6} m/s is more than ten times higher compared to that observed in Figure 7a. Compared to model A, the respective seepage velocities are slightly lower in the upper part of the starter dike, 0.3 x 10^{-6} m/s, to double in the lower part of the starter dike attaining 0.7 x 10^{-6} m/s (Figure 8b). In the gravely base beneath the starter dike, the maximum velocity of 21 x 10^{-6} m/s is due mainly to the concentration of pressure gradient. On the other hand, the horizontal direction of the seepage and the overall highest velocity are observed along the drainage carpet underlying the tailings dam, 335 x 10^{-6} m/s (Figure 8c).

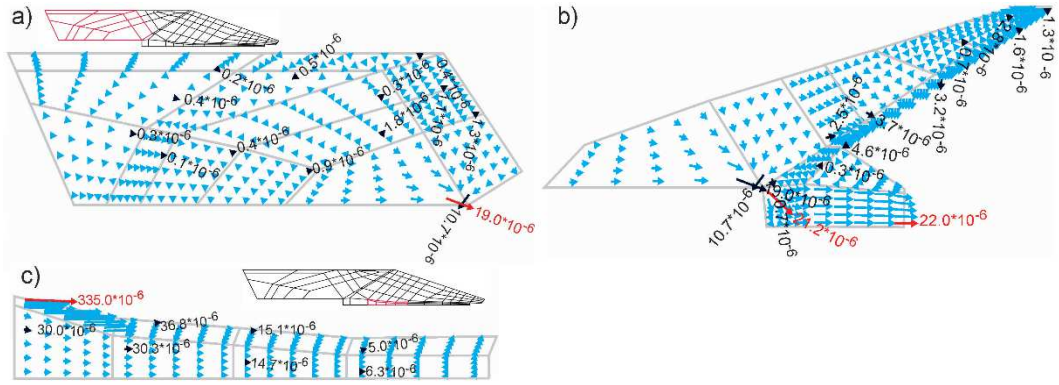

Fig. 8 *Model B: Velocity of seepage (m/s) in characteristic parts of the seepage domain. The maximum velocity value is indicated in red*

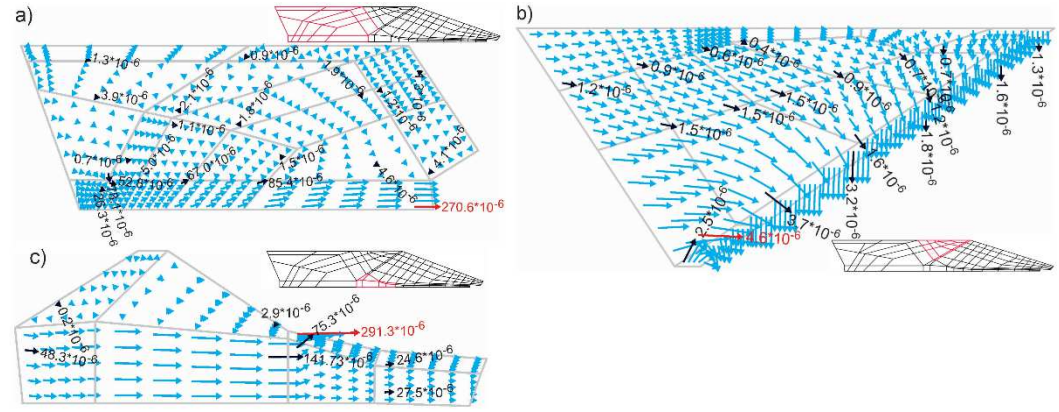

Fig. 9 *Model C: Velocity of seepage (m/s) in characteristic parts of the seepage domain. The maximum velocity value is indicated in re*

Model C: horizontal seepage along the gravely base underlying the tailings pond and the starter dike can be observed. There, the maximum simulated value is 270 x 10^{-6} m/s (Figure 9a). Within the tailings pond, the seepage velocities are higher than that observed in model B. In the starter dike the maximum seepage velocity is 2.9 x 10^{-6} m/s in the zone close to the vertical drain, where the extreme seepage velocity is 291.0 x 10^{-6} m/s, Figure 9c.

5.4 HYDRAULIC GRADIENTS

Figure 10 presents the distribution of the critical hydraulic gradient, which applies to the three considered models. It was calculated for the sand embankment, starter dike and stone fill support by applying the empirical Eq. (1), according to data given in Table 1. The estimated critical hydraulic gradient is below one within the sand embankment, except in the lower part where it varies between 1.0 and 1.4. The critical hydraulic gradient in the domain of the starter dike is, $i_c = 1.2$. The maximum value of the critical hydraulic gradient, $i_c = 1.4$ appears in the lower half of the supporting rockfill.

The distribution of the manifested hydraulic gradients generated by the seepage forces in all three models is shown in Figure 11a, Figure 11b, Figure 12a and Figure 13a.

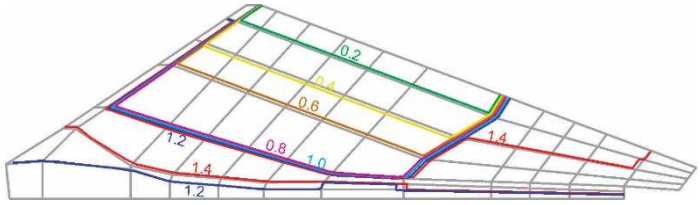

Fig. 10 *Distribution of the critical hydraulic gradient*

Model A: The extreme hydraulic gradient of 5 occurs at the top of the starter dike, (Figure 11a and Figure 11b). Other zones with larger hydraulic gradients can also be observed, such as at the interface starter dike-send embankment-vertical drain with a value of 3. A few such zones are also located at the downstream slope of the sand embankment, varying between 1 and 3. A larger hydraulic gradient also occurs the toe of the drainage carpet and the outlet channel at the bottom age of the supporting rockfill. It is now possible to evaluate the zones which are critical for the erosion of soil particles. They are completed when the ratio between the manifested (actual) hydraulic gradient and the allowable critical hydraulic gradient is higher than one (Figure 11c and Figure 11d). Several such zones can be observed: (i) at the top of the starter dike (ratio=4), (ii) on the downstream face of the sand embankment (ratio=10~15), and (iii) the zone at the interface of the sand embankment with the drain carpet at the downstream edge of the model (ratio=3). In addition to the high ratio, the erosion potential builds up when seepage occurs through cracks or compaction deficiencies in the upper relatively poorly compacted layers of the sand embankment.

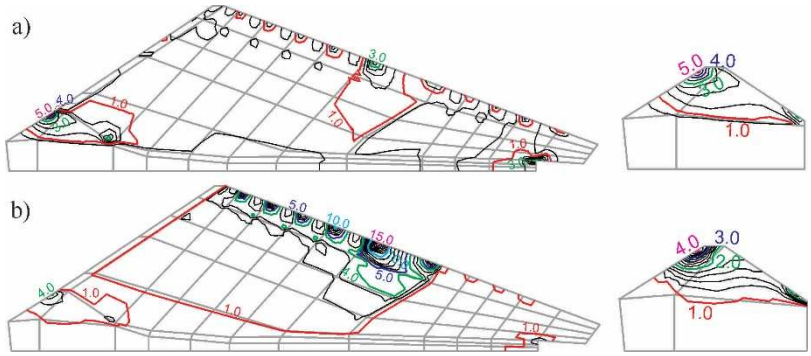

Fig. 11 *Model A: a) manifested hydraulic gradients in the sand embankment, the starter dike and in the stone fill support (equidistance 0.5), and manifested hydraulic gradients in the starter dike only (equidistance 0.5), b) critical zones for soil erosion, computed as the ratio between the actual and critical hydraulic gradients, in the sand embankment and in the starter dike (equidistance 1), and critical zones for soil erosion in the starter dike only (equidistance 0.2)*

This means that hydraulic instability of the respective critical zones can endanger the stability of the entire dam. However, in well compacted soil environments, the critical gradient threshold can be increased by as much as 70% with respect to values given in Eq. (1). Also, the presence of friction forces between the soil parts further opposes the movement of the particles. Consequently, the potential for erosion can be reduced respectively.

Model B: As opposed to model A, where the maximum manifested hydraulic gradient occurs at the upper part of the starter dike, here the maximum manifested hydraulic gradient occurs at the bottom of the starter dike at the upstream slope with a magnitude of 6.5 (Figure 12a). Actually, in the whole domain of the starter dike, the manifested hydraulic gradient is larger than the allowable value of 1.2. The only exception is at the crown of the starter dike where the

manifested hydraulic gradient equals the allowable. At the same time, the most critical zone for erosion appears at the bottom of the starter dike with a 5.4 times higher ratio than the allowable, Figure 12b. Although the critical gradient value increases by 70% in the well compacted soil just like the starter dike, assuming that in this zone the potential of erosion is additionally reduced due to the presence of friction forces between the soil particles that further oppose their movement, the potential of erosion still exists.

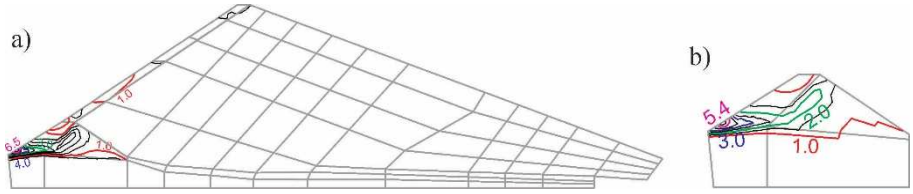

Fig. 12 *Model B: a) manifested hydraulic gradient in the starter dike and sand embankment (equidistance 0.5); b) critical zones for soil erosion in the starter dike (equidistance 0.5)*

Contrary to the seepage model A, where the most critical zone appears in the upper part of the dike, in the case of model B, it appears at the lower part of the starter dike close to the natural gravely sediments, which makes the hydraulic instability less likely to occur.

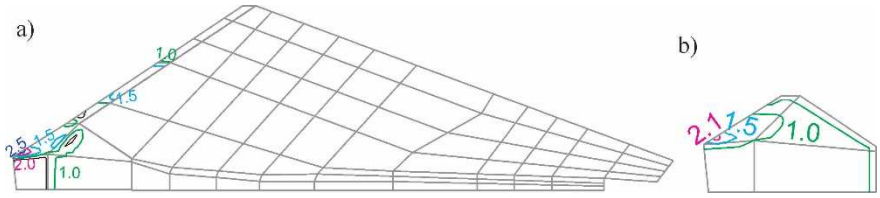

Fig. 13 *Model C: a) manifested hydraulic gradient in the starter dike and sand embankment and b) critical zones for soil erosion in the starter dike (equidistance 0.5)*

Model C: Similar to model B, the maximum manifested hydraulic gradient of 2.5 occurs at the bottom of the starter dike at the upstream slope (Figure 13a). The remaining parts of the starter dike have a hydraulic gradient close to the allowable. The critical zone for the erosion potential with a ratio of 2.1 times higher than the allowable is visible in Figure 13b. However, respecting the substantial compaction in this zone as well as the positive impact of friction between the soil particles, this potential becomes insignificant.

5.5 HEAVE POTENTIAL (STATIC LIQUEFACTION)

Static liquefaction or heave occurrence can trigger dam failures, manifested via internal erosion and/or slope instability. The heave effect is mainly generated by confined seepage flow concentrated in a high permeability layer overlaid by a low permeability layer, under conditions of first filling of the reservoir, as well as in cases of pore pressures increase due to erosion or suffusion, or blockage of drains and pressure relief walls. In the considered tailings dam, the latter two phenomena can initiate heaving as a balance problem between upward pore water pressure due to buoyancy force and downward static loads resulting in zero-effective stress. At the soil particle level, the pressure force acts outward, uniformly in all directions, whereas the spherical stress acts in the same manner, but in the opposite (inward) direction. The heave potential F can then be expressed by the following equation:

$$F = \frac{\sigma_0}{U} \tag{9}$$

where σ_0 is the total spherical (mean) stress and U is the pore water pressure at the same stress point for flow in both horizontal and upward direction.

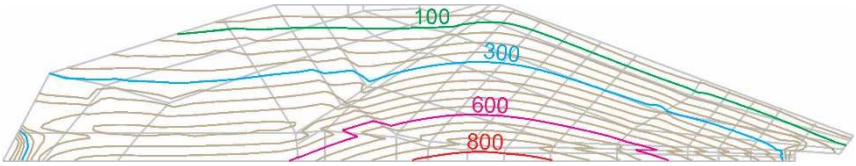

Fig. 14 *Total spherical static stresses σ_0 (kPa). Equidistance is 50 (kPa)*

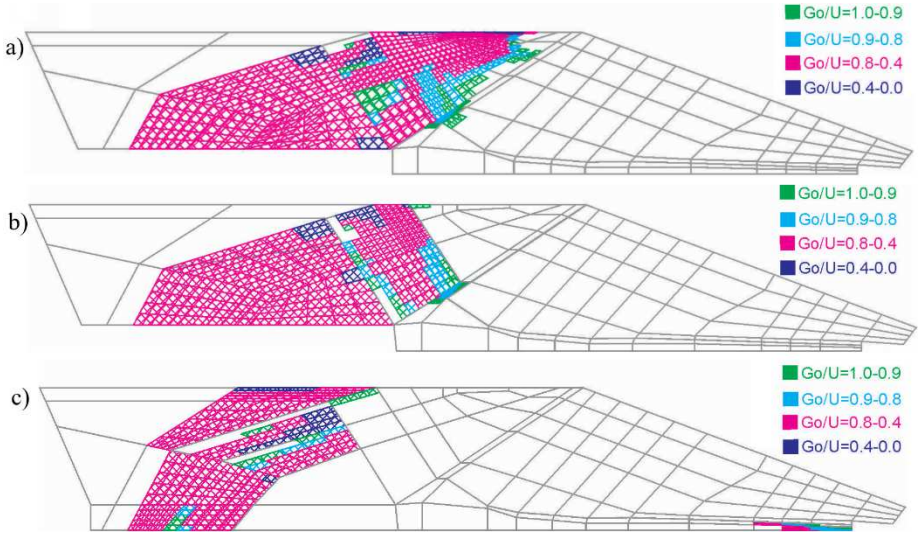

Fig. 15 *Heave potential (static liquefaction) for a) model A, b) model B, and c) model C*

Accordingly, static liquefaction in the form of a heave effect is possible in zones where the ratio between the spherical total stress and the pore pressure becomes equal to or lower than 1. In the present analysis, a factor of safety against heave of 1,5 is assumed to be compatible with the degree of uncertainty of the prediction pressure. The single lift static analysis conducted herein is based on the ideal elasto-plastic Mohr-Coulomb material model considering zones of increasing soil stiffness with depth. Since the softer soils of the dam start to exhibit nonlinear behaviour with the beginning of the loading, the stress state is defined considering the secant modulus corresponding to 50% of the soil strength E_{50}, for each distinct soil stiffness zone. Figure 14 depicts the distribution of the total spherical static stresses for the example tailings dam-impoundment system.

Figure 15 shows the heave potential for the three seepage models. For model A, the small σ_0/U ratio in the range of 0.4~0.8, indicates that static liquefaction may occur in a large part of the tailings impoundment (Figure 15a). Near the upstream slope of the starter dike, just below the crest, and in a narrow zone of send embankment in the vicinity to the downstream slope of the starter dike, the ratio varies in the range of 0.9~1.0, whereas above the starter dike the ratio decreases slightly in the range of 0.8~0.9. The seepage model B displays a similar heave potential as that of model A (Figure 15b). However, whereas the starter dike and the sand embankment above the dike crest exhibit similar heave potentials, the upper part of the impoundment near the upstream slope of the sand embankment appears not affected at all. In the case of model C, the heave potential is simulated only partially in the impoundment zones, distanced from the upstream slopes of the starter dike and sand embankment, and doesn't appear to impact the stability of the tailings dam-impoundment system (Figure 15c).

6. CONCLUSIONS

An analytical study of the seepage related processes was conducted for a tailings dam-impoundment system with and without a lining option. The following parameters were considered: the potential field, pore pressure distribution, seepage velocities, critical and manifested hydraulic gradients, and the potential for piping initiated by erosion and the heave effect. To demonstrate their importance in the hydrodynamic dam stability, an existing tailings dam-impoundment system was analysed for three different seepage boundary conditions: model A (lining installed on the reservoir walls, reservoir bottom and on the upstream slope of the starter dike); model B (lining of the reservoir walls and the reservoir bottom); and model C (no lining).

The critical hydraulic gradient reflects the soil inherent properties and the compaction effect, while the manifested (actual) hydraulic gradient reflects the soil permeability and seepage conditions. Critical zones with potential for internal erosion were identified when the ratio between the manifested hydraulic gradient and the critical hydraulic gradient was larger than one. For model A, critical zones were the top of the starter dike (ratio=4), the downstream slope of the sand embankment (ratio=10∼15), and the interface of the sand embankment with the drain carpet at the downstream edge of the model (ratio∼3). Model B displayed critical zones for erosion at the bottom of the starter dike (ratio=5.4), which, being on top of the natural gravely sediments, is less prone to hydraulic instability. Model C showed the lowest potential for erosion, insignificant for tailings dam stability. Model A had also the highest susceptibility to static liquefaction, whereas the hydrodynamic stability of model C was not affected since the detected liquefiable zones in the impoundment were located far from the upstream face of the starter dike and sand embankment.

The main conclusion of the seepage analyses is that the installation of the impermeable lining can have a significant impact on the seepage velocities and pore pressure distribution and can initiate hydrodynamic instability of the tailings dam. Therefore, when local environmental settings require protection with seepage barriers, a comprehensive engineering assessment of the expected negative hydrodynamic effects has to be made.

7. REFERENCES

[1] P.N. Psarropoulos, Y. Tsompanakis, Stability of tailings dams under static and seismic loading, *Canadian Geotechnical Journal*, Vol. 45, No. 5, pp. 663-675, 2008. https://doi.org/10.1139/T08-014

[2] S. Hu, Y. Chen, W. Liu, S. Zhou, R. Hu, Effect of seepage control on stability of a tailings dam during its staged construction with a stepwise-coupled hydro-mechanical model, *International Journal of Mining Reclamation and Environment*, Vol. 29, No. 2, pp. 125–140, 2015. https://doi.org/10.1080/17480930.2013.870693

[3] C. Liu, Z. Shen, L. Gan, L. Xu, K. Zhang, T. Jin, The Seepage and Stability Performance Assessment of a New Drainage System to Increase the Height of a Tailings Dam, *Applied Sciences*, Vol. 8, No. 10, pp. 1840, 2018. https://doi.org/10.3390/app8101840

[4] A. Daouadji, P.Y. Hicher, An enhanced constitutive model for crushable granular materials, *International Journal for Numerical and Analytical Methods in Geomechanics*, Vol. 34, No. 6, pp. 555–580, 2009. https://doi.org/10.1002/nag.815

[5] A. Small, J. Herza, M. Ashley, J. Thorp, A consequence-based tailings dam safety framework, *Proceedings of the ICOLD 2019 Symposium - Sustainable and Safe Dams Around the World*, 9-14 June 2019, Ottawa, Canada, ISBN 9780367334222.

[6] D.Q. Deng, L. Liu, Z.L. Yao, K.I.-I.L. Song, D.Z. Lao, A practice of ultra-fine tailings disposal as filling material in a gold mine, *Journal of Environmental Management*, Vol. 196, pp. 100–109, 2017. https://doi.org/10.1016/j.jenvman.2017.02.056

[7] WISE Uranium Project: Chronology of major tailings dam failures, http://www.wise-uranium.org/mdaf.html, 2023.

[8] S. Azam, Q. Li, Tailings dam failures: A review of the last one hundred years, *Geotechnical News*, Vol. 28, pp. 50–54, Corpus ID: 42486740, 2010.

[9] L. Zongjie, C. Junrui, X. Zengguang, Q. Yuan, C. Jing, A Comprehensive Review on Reasons for Tailings Dam Failures Based on Case History, *Advances in Civil Engineering*, Vol. 2019, pp. 18, Article ID 4159306, 2019. https://doi.org/10.1155/2019/4159306

[10] M. Foster, R. Fell, M. Spannagle, The statistics of embankment dam failures and accidents, *Canadian Geotechnical Journal*, Vol. 37, No. 5, 2000. https://doi.org/10.1139/t00-030

[11] ANCOLD Guidelines on Tailings Dams, Australian National Committee on Large Dams, 2012.

[12] Canadian Dam Association (CDA), Technical Bulletin, Application of Dam Safety Guidelines to Mining Dams, 2014.

[13] T. Wang, Y. Zhou, Q. Lv, Y. Zhu, C. Jiang, A safety assessment of the new Xiangyunphospho gypsum tailings pond, *Minerals Engineering*, Vol. 24, No. 10, pp. 1084–1090, 2011. https://doi.org/10.1016/j.mineng.2011.05.013

[14] L. Dong, D. Sun, X. Li, Theoretical and case studies of interval non probabilistic reliability for tailing dam stability, *Geofluids*, Vol. 2017, pp. 11, Article ID 8745894, 2017. https://doi.org/10.1155/2017/8745894

[15] A. Bjelkevik, S. Knutsson, Swedish tailings: Comparison of mechanical properties between tailings and natural geological materials, *Proceedings of Securing the Future International Conference on Mining and The Environment*, *Metals and Energy Recovery*, Skelleftee, Sweden, 2005.

[16] J.F. Lupo, K.F. Morrison, Innovative geosynthetic liner design approaches and construction in the mining industry, *Proceedings of Geo-Frontiers Congress*, Austin, Texas, United States, January 24-26, 2005. https://doi.org/10.1061/40787(166)18

[17] K.S. Richards, K.R. Reddy, Critical appraisal of piping phenomena in earth dams, *Bulletin of Engineering Geology and the Environment*, Vol. 66, No. 4, pp. 381-402, 2007. https://doi.org/10.1007/s10064-007-0095-0

[18] D.S. Chang, L.M. Zhang, Extended internal stability criteria for soils under seepage, *Soils and Foundations*, Vol. 53, No 4, pp. 569-583, 2013. https://doi.org/10.1016/j.sandf.2013.06.008

[19] R. De Jager, The behaviour of solids during static liquefaction in Geotechnical engineering, Master thesis Delft University of Technology, Netherlands, 2006.

[20] A.B. Fourie, L. Tshabalala, Initiation of static liquefaction and the role of K0 consolidation, *Canadian Geotechnical Journal*, Vol. 42, No. 3, pp. 892-906, 2011.

https://doi.org/10.1139/t05-026

[21] B. Indraratna, S. Radampola, Analysis of Critical Hydraulic Gradient for Particle Movement in Filtration, *Journal of Geotechnical and Geoenvironmental Engineering*, Vol. 128, No. 4, pp. 347-350, 2002. https://doi.org/10.1061/(ASCE)1090-0241(2002)128:4(347)

[22] K.S. Richards, K.R. Reddy, True Triaxial Piping Test Apparatus for Evaluation of Piping Potential in Earth Structures, *Geotechnical Testing Journal*, Vol. 33, No. 1, pp. 83–95, 2010. https://doi.org/10.1520/GTJ102246

[23] C.F. Wan, R. Fell, Investigation of Rate of Erosion of Soils in Embankment Dams, *Journal of Geotechnical and Geoenvironmental Engineering*, Vol. 130, No. 4, pp, 373–380, 2004. https://doi.org/10.1061/(ASCE)1090-0241(2004)130:4(373)

[24] J.H. Schmertmann, The Non-Filter Factor of Safety Against Piping Through Sand, *Proceedings of Geo-Congress' 98, ASCE Geotechnical Special Publication 111*, Reston, VA, pp. 65-132, 2015. https://doi.org/10.1061/9780784405376.006

[25] X. Quanyi, L. Jian, H. Bo, L. Hongtao, L. Yuying, L. Xuanzheng, Critical Hydraulic Gradient of Internal Erosion at the Soil–Structure Interface, *Processes*, Vol. 6, No. 7, pp. 92, 2018. https://doi.org/10.3390/pr6070092

[26] I. Jahanzaib, B. Indraratna, Study of Critical Hydraulic Gradients for Seepage-Induced Failures in Granular Soils, *Journal of Geotechnical and Geoenvironmental Engineering*, Vol. 145, No. 7, 2019. https://doi.org/10.1061/(ASCE)GT.1943-5606.0002062

[27] C.F. Wan, R. Fell, Assessing the potential of internal instability and suffusion in embankment dams and their foundations, *Journal of Geotechnical and Geoenvironmental Engineering*, Vol. 134, No. 3, pp. 401-407, 2008. https://doi.org/10.1061/(ASCE)1090-0241(2008)134:3(401)

[28] K. Terzaghi, R.B. Peck, *Theoretical Soil Mechanics in Engineering Practice*, A Wiley Inter Science Publication, John Wiley & Sons Inc., New York, 1948.

[29] S. Perzlmaier, Distributed filter speed measurement in dams (in German), Ph.D. Thesis, Technical University of Munich, Germany, 2007.

[30] ADAD-IZIIS software, Analysis and design of arch dams – User's manual, Institute of Earthquake Engineering and Engineering Seismology – IZIIS, University of Ss. Cyril and Methodious, Skopje, R. N. Macedonia, 2018.